

## Slippery flows of a Carbopol gel in a microchannel

Eliane Younes,<sup>1,\*</sup> Volfango Bertola ,<sup>2,†</sup> Cathy Castelain,<sup>1,‡</sup> and Teodor Burghelca <sup>1,§</sup><sup>1</sup>Université de Nantes, CNRS, Laboratoire de Thermique et Énergie de Nantes, LTeN, F-44000 Nantes, France<sup>2</sup>Laboratory of Technical Physics, School of Engineering, University of Liverpool, Liverpool L69 3GH, United Kingdom

(Received 3 February 2020; accepted 22 July 2020; published 19 August 2020)

The ability to predict and/or control wall slip is a fundamental problem in the hydrodynamics of yield stress fluids, which is poorly understood to date and has important applications in bio- and microfluidic systems. Systematic measurements of steady flows of a simple yield stress fluid (Carbopol Ultrez 10) in a plane acrylic microchannel are used to establish rigorous scaling laws for the wall velocity gradient and the slip velocity. By means of epifluorescent microscopy combined with a custom-developed digital particle image velocimetry technique, time series of velocity fields were measured within a wide range of flow rates, and three distinct flow regimes were identified: full plug, partial plug, and fully yielded. Corresponding to each flow regime, wall velocity gradients and slip velocities were obtained by extrapolating the velocity profiles using a smoothing spline function. By combining the flow-field measurements with the macro-rheological measurements, scaling laws for the wall velocity gradient and the slip velocity with the wall shear stress were identified and compared with results from the literature. Detailed microscopic measurements of the velocity field enabled an assessment of the effectiveness of a chemical treatment of the channel walls meant to suppress wall slip proposed by Metivier and co-workers [Soft Matter 8, 7365 (2012)].

DOI: [10.1103/PhysRevFluids.5.083303](https://doi.org/10.1103/PhysRevFluids.5.083303)

A ubiquitous phenomenon observed during flows of yield stress materials along smooth solid surfaces is the slip of the velocity near the wall. From a phenomenological standpoint it is believed that the wall slip originates from the presence of a depleted layer of solvent near the solid surface, and the bulk of the material “slides” over it. Some qualitative observations of the slip layer performed particularly for solid suspensions do exist [1,2]. With regard to Carbopol dispersions, such observations are, to the best of our knowledge, practically absent in the literature.

As compared to the case of slip during flows of molecular (simple, or Newtonian) fluids where, based on the precise knowledge of the intermolecular forces, a rigorous theoretical framework may be derived [3,4], the wall slip of yield stress materials remains elusive. A key step in understanding the physics of the wall slip in yield stress fluids is to reliably measure scaling laws of the slip velocity with respect to the wall shear stresses and the wall velocity gradients. The scaling behavior during flows of yield stress fluids in the presence of wall slip remains, however, an open topic. To substantiate this statement, we present in the following a brief literature review. The existing studies of wall slip during flows of yield stress fluids along smooth solid surfaces may be grouped into three distinct classes.

\*Eliane.Younes@univ-nantes.fr

†Volfango.Bertola@liverpool.ac.uk

‡Cathy.Castelain@univ-nantes.fr

§Corresponding author: Teodor.Burghelca@univ-nantes.fr

The first class refers to phenomenological modeling and/or numerical studies of the wall slip phenomenon [5,6]. Such studies typically rely on assumptions concerning the microstructure of the material in the vicinity of the solid wall, which are often difficult to probe by means of direct visualization. As the numerical studies are concerned, the evolution of the velocity gradients and stresses near the wall is typically obtained by assuming a known bulk rheological behavior of material. Depending on the phenomenological assumptions being made, various slip laws are derived. The agreement between various phenomenological scaling predictions is, to the best of our understanding, not very satisfactory in the sense that various authors obtain different scaling results even when the same material is concerned, which rarely match the experimental results [5,6].

A second and significantly broader class of studies refers to macroscopic experiments performed in either rheometric [7–13] or nonrheometric [14,15] geometries. Such studies are sometimes combined with rather simple phenomenological models, and scaling laws are obtained. The presence of wall slip complicates the determination of the yield stress [16] and systematically biases the assessment of the solid-fluid transition [14,17].

A systematic experimental study of the wall slip phenomenon in a rheometric flow was reported by Meeker and co-workers [7]. By assessing the slip behavior via macrorheological tests combined with measurements of the velocity geometry within the gap of the rheometric geometry, they identify three distinct slip regimes. They observed wall slip for applied stresses close to the yield stress  $\tau_y$ , whereas in a fully yielded regime this effect was negligible. A second macrorheological study of the wall slip observed during flows of hard-sphere colloidal glasses was reported by Ballesta and co-workers [9]. This study highlights only two slip regimes: solid ( $S$ ) and fluid ( $F$ ). Within the regime ( $S$ ) a Bingham-type slip regime is observed, whereas within the ( $F$ ) regime a Herschel-Bulkley slip behavior is observed.

The experimental study by Meeker and co-workers [7] is complemented by a phenomenological model based on the microelastohydrodynamic lubrication picture, which allows one to derive scaling laws for the full slip case. The main assumption behind this phenomenological approach is the existence of a depleted layer of solvent of width  $\delta$  in the vicinity of the solid surface. However, the authors note that “*the slip layer is not resolvable in our setup, indicating that its thickness is smaller than 50  $\mu\text{m}$* ” meaning that during their experiments this assumption could not be probed by direct observation. A similar estimate of the layer thickness has been reported by Zhang and co-workers [11]. Such small values explain why a direct visualization of the depleted layer of solvent has never been reported in the literature.

A second subclass of experimental macroscopic studies refers to nonrheometric flows such as laminar pipe flows. A study of the flow in the presence of wall slip in a glass-made capillary tube of a 0.2 wt. % Carbopol gel was performed by Pérez-González *et al.* [15]. By combining the particle image velocimetry technique with classical rheological measurements, they found that the solid-fluid transition occurs gradually, which complicates the determination of the yield stress. The authors estimate the wall velocity gradients using the relation between the imposed flow rate  $Q$  and the analytical solution of a fully developed Poiseuille flow for a Newtonian fluid. An experimental study of a laminar flow of a Carbopol gel in a glass-made cylindrical pipe with a radius  $R = 1.9$  mm was performed by Poumaere and his co-workers [14]. Several important findings of this study can be summarized as follows. First, consistently with the findings of Pérez-González and co-workers, the transition from a solidlike to a fluidlike regime is smooth and mediated by an intermediate regime where the solid and fluid behaviors coexist. Second, the wall slip effects were found to be more pronounced around the yield point.

A third class of studies refers to microscopic flows where the influence of the confinement is expected to play an important role and cannot be decoupled from the wall slip and yielding behavior [18–21]. As compared to the second class, this third class of studies is somewhat less represented, although the microscopic wall slip behavior is relevant to a number of microscopic experimental settings such as the impact and/or atomization of viscoplastic drops [22–25] with a number of applications in fuel industry and microscopic blood flows [26,27].

Geraud *et al.* [19] studied the influence of confinement on the flow of a Carbopol microgel. They compare the bulk rheological behavior assessed via macroscopic rheological tests and the velocity profiles measured in rough microchannels. They found a strong disagreement between the bulk prediction of the velocity profiles and the ones measured in the microchannels, and they attribute this discrepancy to the confinement of the flow. Liu *et al.* [18] compared the measured velocity profiles in microchannels to simulations performed based on the bulk rheology. They show that the confinement effects become important when the dimensions of the channel are comparable to the characteristic size of the material's microstructure, and consequently the measured velocity profiles differ from those computed numerically using the Herschel-Bulkley constitutive relation. These studies address the effects of the confinement on the flow behavior and provide some information on the wall slip phenomenon as well.

Most recently, Péméja and co-workers have presented a systematic experimental investigation of wall slip regimes of a Carbopol gel in a microchannel [21]. As in Ref. [15], the authors compute the wall shear stress using the pressure drop. To rationalize their results, the authors use a phenomenological model similar to the one proposed by Meeker and co-workers in Ref. [7]. Based on measurements of the transversal profiles of the axial velocity, they identify two distinct scaling regimes as the driving pressure drops are gradually increased. Seth and co-workers studied the slip behavior in a microscopic rotational shear cell (Linkam CSS 450) by means of particle tracking velocimetry [28]. They identify two slip regimes separated by an abrupt transition. For stresses exceeding the yield stress  $\tau > \tau_y$ , the slip velocity scales linearly with the stress, and the slope of this linear dependence does not depend on the chemistry of the solid surface. In the plug flow regime ( $\tau < \tau_y$ ), the slip velocity measured at an imposed stress is very sensitive to the nature of the surfaces. To rationalize their findings, the authors use an elastohydrodynamic lubrication model that allows them to compute the wall shear stress as a function of the slip velocity and the thickness  $\delta$  of the lubricating layer. A microscopic study of the slip behavior of a soft glassy material is presented by Mansard and co-workers [29]. They highlighted a strong dependence of the slip behavior on the degree of roughness of the solid surface, which was accurately controlled by means of micropatterning using a standard microphotolithography procedure.

An important conclusion that can be drawn from the existing experimental studies performed in macroscopic or microscopic geometries is that the wall slip behavior cannot be de-coupled from the yielding behavior. Unlike in the case of the polymer melts where the wall slip emerges at large rates of strain [30,31], in the yield stress materials the picture is strikingly different. All the experiments reviewed above indicate that the wall slip effects are more pronounced in a range of low shear rates (where the solid-fluid transition takes place) and are significantly less important far beyond the yield point when a simple constitutive equation (such as the Herschel-Bulkley constitutive law) is reliable [14,17]. Whereas there seems to be a general consensus about this fact within the viscoplastic community, various authors use different assumptions (which in most of the cases could not be verified by means of direct visualization of the flow in windows sufficiently small and close to the solid boundary) and phenomenological models (e.g., the elastohydrodynamic lubrication model sometimes combined with yet other assumptions on the nature of intermolecular forces responsible for the wall slip) in order to rationalize their findings and obtain scaling laws. An additional drawback of some of the previous studies relates to using questionable correlations (e.g., computing the wall shear rate using the flow rate or preassuming a Herschel-Bulkley-like velocity profile, which, as shown in Ref. [18], is not accurate in the presence of confinement). The overall conclusion is that, in spite of the reliability of the macroscopic scale experiments in capturing the wall slip behavior, there seems to exist no universal consensus on either the scaling behavior or the fundamental physical mechanisms responsible for the wall slip behavior.

The central aim of the present contribution is to provide a systematic experimental characterization of the microscopic wall slip phenomenon in terms of scaling laws of the slip velocity with both the wall shear stresses and the wall velocity gradients. The novelty of the approach we propose in the following consists of assessing these scaling laws by judiciously correlating microscopic

measurements of the wall velocity gradients performed in a plane microchannel with the bulk rheological behavior assessed by macrorheological measurements performed in a steady state. By doing so, we avoid making any of the assumptions other authors made, such as the presence of a lubricating layer and/or a constitutive relation and/or the relationship between the wall shear stresses and the driving pressures. The study is complemented by an investigation of the effectiveness of a chemical treatment of the channel walls meant to suppress the wall slip.

The paper is organized as follows. The rheological characterization of the working fluid is presented in Sec. I A. The design of the microchannel setup as well as the data acquisition protocol are presented in Sec. I B. The data analysis procedure is discussed in Sec. I C. A systematic characterization of the velocity profiles is presented in Sec. II. By combining the microfluidic and macrorheological measurements, we identify in Sec. II B different scaling laws of the wall slip phenomenon corresponding to different flow regimes. A detailed comparison of the experimentally found scaling laws with the results from the literature is presented in Sec. II C. In Sec. III we explore the possibility of inhibiting the wall slip via a chemical treatment of the microchannels. The paper closes in Sec. IV with a summary of the main conclusions and a discussion of several perspectives this study may open.

## I. EXPERIMENTAL METHODS

### A. Choice, preparation, and rheological characterization of the working fluid

We chose a Carbopol gel as a working fluid. The rationale behind this choice is the following. First, such gels are optically transparent, which allows an *in situ* visualization of their flows and subsequent measurements of the flow fields. Second, they are chemically stable over extended periods of time. Third, and foremost, the Carbopol gels have been considered as “*model*” yield stress materials for over two decades [32–34]: they exhibit almost no thixotropy and their deformation may be described by the Herschel-Bulkley law.

However, it has been shown recently that even in the case of a Carbopol gel, the solid-fluid transition does not occur at a well-defined value of the applied stress but gradually (within a finite range of stresses and, when forced in an unsteady fashion, they equally exhibit weak thixotropic effects manifested through a rheological hysteresis that is related to the degree of steadiness of the forcing [25,35–39]). In addition, the Herschel-Bulkley constitutive relationship cannot reliably describe the deformation states within the transitional regime.

To avoid such time-dependent effects that may bias the slip behavior, we focus throughout this paper on steady-state microscopic flows, which we correlate to steady-state rheological measurements.

#### 1. Fluid preparation

The working fluid was an aqueous solution of Carbopol Ultrez 10 with the concentration of 0.1 wt. %. Carbopol is the generic trade name of a cross-linked polyacrylic acid  $-\text{[CH}_2 - \text{CH(COOH)]}-$  with high molecular weight. In an anhydrous state, it is commercialized in the form of a white powder soluble in aqueous solvents. After the addition of a neutralizing agent such as sodium hydroxide (NaOH), a clear gel is obtained. The Carbopol gels exhibit an elastoviscoplastic rheological behavior in a neutral state due to the presence of a jammed spongy microstructure [36,40,41].

The Carbopol gel was prepared according to the following protocol. First, the right amount of anhydrous Carbopol was dissolved in deionized water using a magnetic stirring device at a speed of 1000 rpm. The degree of mixing/dissolution was assessed visually by monitoring the optical isotropy of the solution. Next, the pH of the solution was gradually increased from 3.2 to 7 by gradual titration with a small amount of a 10 wt. % aqueous NaOH solution gradually pipetted while gently mixing the solution. The rheological tests were performed after seeding the Carbopol

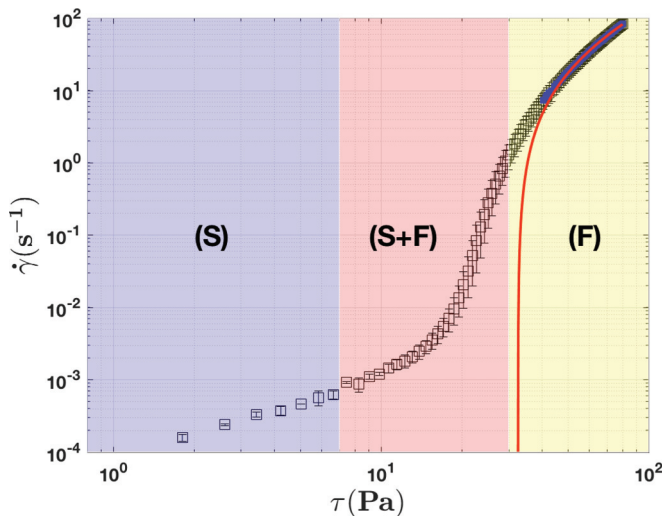


FIG. 1. Dependence of the shear rate  $\dot{\gamma}$  on the applied stress  $\tau$ . The red line represents the Herschel-Bulkley fit that gives  $\tau_y = 32.5 \pm 2.5$  Pa,  $K = 2.8 \pm 0.215$  Pa s $^n$ ,  $n = 0.6403 \pm 0.0299$ . The symbols marking the highlighted regions denote the deformation regimes and are explained in the text: (S), solid; (S + F), solid-fluid coexistence; (F), fluid.

solution with the fluorescent tracers as detailed in Sec. IB. The average density of the Carbopol solution measured at room temperature was  $\rho \approx 1100$  kg m $^{-3}$ .

## 2. Rheological measurements

The rheological measurements were performed using a controlled stress rotational rheometer (Mars III, Thermofischer Scientific) equipped with a nanotorque module. Tests were performed using a parallel plate geometry with a diameter  $D = 35$  mm and a gap  $d = 1$  mm. To prevent the wall slip, glass paper with an average roughness of  $500$   $\mu\text{m}$  was glued on each plate. To account for the addition of the glass paper on the rotating plate of the device, the inertia of the device was recalibrated. The absence of any wall slip effect was verified by measuring flow curves in subsequent tests performed with several values of the gap and showing that all measurements perfectly overlap. To prevent the evaporation of the solvent during the rheological measurements, a thin layer of commercial oil was added to the free meniscus of the sample.

Rheological measurements were performed according to the following protocol. First, the sample was presheared at a constant applied stress larger than the yield stress for 300 s and allowed to relax for another 300 s. Then, to assess the rheological behavior of the Carbopol gel in different deformation regimes, a commonly used rheological test consisting of loading the material according to an increasing stress ramp was applied to a fluid sample. The duration of each step was  $t_0 = 5$  s and the data averaging time per stress value was  $\delta t_0 = 2$  s.

To test the reproducibility and quantitatively assess the instrumental error, each rheological measurement was repeated three times with a fresh sample. A rheological flow curve obtained by averaging the results of three distinct measurements is illustrated in Fig. 1. The error bars are defined by the standard deviation of the three datasets.

Three distinct deformation regimes consistent with previous macrorheological investigations [25,36–39,42] are observed. For low values of applied stress, the variation of the rate of material deformation  $\dot{\gamma}$  with the applied stress is negligibly small. This corresponds to a solidlike behavior of the material [region (S) in Fig. 1]. For high values of applied stress (beyond the yield stress), the

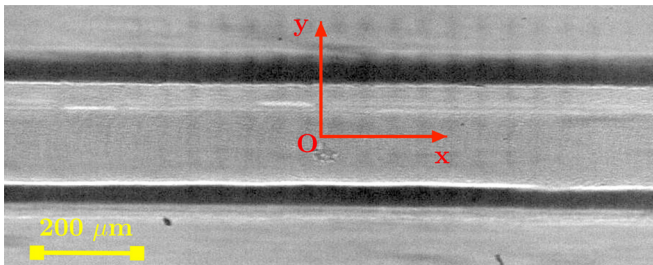


FIG. 2. Micrograph of the microchannel. The image was acquired in white light.

material becomes fully yielded [region ( $F$ ) in Fig. 1], and its behavior follows the Herschel-Bulkley fit (red line in Fig. 1).

For intermediate values of the applied stresses, the solid-fluid transition is not direct and the behavior of the material corresponds neither to a solidlike regime nor to a viscous flow regime [region ( $S + F$ ) in Fig. 1]. Based on the Herschel-Bulkley fit, the yield stress of the working material is around  $\tau_y \approx 32.5$  Pa.

A natural question one may ask at this point is to what extent the steady-state rheological measurements presented in Fig. 1 are relevant to the steady microchannel flow under investigation. As shown in Refs. [25,36] for characteristic times per stress step  $t_0$  larger than  $2s$  (we recall that the rheological data were acquired with  $t_0 = 5$  s), the regimes ( $F$ ) and ( $S + F$ ) are practically independent of  $t_0$  while a weak dependence is always observed in the regime ( $S$ ). This means that as long as we restrict ourselves to the regimes ( $F$ ) and ( $S + F$ ), a meaningful correlation between the rheological measurements presented in Fig. 1 and the flow fields measured in the microchannel can be made. For a more systematic analysis of the influence of the rate at which Carbopol gels are loaded during controlled stress ramps on the rheological response, the reader is referred to Refs. [25,43].

### B. Microchannel design, microscopic flow control, and data acquisition protocol

The experiments have been performed in a straight microchannel. The width of the microchannel is  $W = 200 \mu\text{m}$ , its depth is  $H = 200 \mu\text{m}$ , and its length is  $L = 4$  cm. A micrograph of the channel is presented in Fig. 2.

The microchannel was machined in an acrylic block with dimensions  $5 \text{ cm} \times 3 \text{ cm} \times 0.5 \text{ cm}$  using a fast spinning (14 000 rot/min) micromilling head (Nakanishi, model HES 510-BT40) mounted on a commercial computer-controlled milling machine (Twinhorn, model VH1010). By a precise alignment of the initial acrylic block on the stage of the milling machine, the depth of the microchannel was uniform over its entire length, with an end-to-end variation smaller than 1%. The average roughness of the edges of the microchannel that resulted from the micromilling process is roughly of the order of a micron, which accounts for a half-percent of the channel width. This point is fully supported by the micrograph of the microchannel shown in Fig. 2. We note that this level of edge smoothness is comparable to that obtained via the classical microlithography techniques used to produce PDMS microchannels [44]. The microchannel was sealed with a strong and optically transparent adhesive tape (3M, model 727-1280). The microchannel chip is mounted on an inverted epifluorescent microscope (Axio Observer A1, serial no. 3832002215) (Fig. 3).

The microscopic flows have been visualized through a  $20\times$  magnification objective (Zeiss EC Plan-NEOFLUAR  $20\times/0,5$ ) with a numerical aperture  $NA = 0.35$  and a long working distance  $WD = 70$  mm. The microscopic flows were generated using a high-precision microsyringe pump (KdScientific, model Legato 110). To ensure a steady flow rate  $Q$ , which was crucial for this study, we have used a 10 mL gas tight syringe (Hamilton, model 1010LT). The flows were illuminated with a powerful halogen lamp coupled to the inverted microscope. To visualize the flow, the working

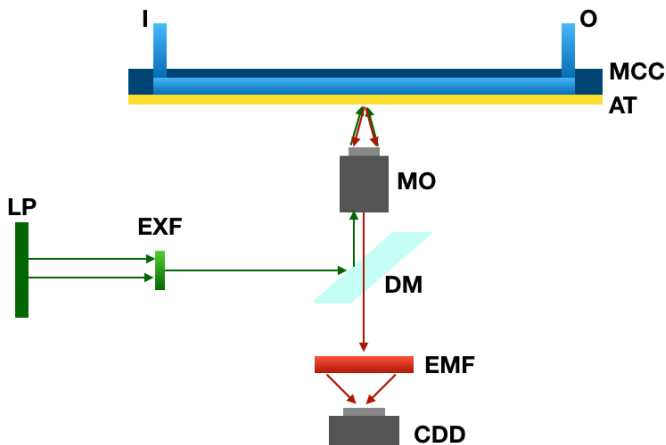


FIG. 3. Schematic view of the microfluidic experimental setup: MCC: microchannel chip, I: microchannel inlet, O: microchannel outlet, AT: adhesive tape, MO: microscope objective, DM: dichroic mirror, LP: light emitting lamp, EXF: excitation filter, EMF: emission filter, CCD: digital camera.

fluid was seeded with a minute amount of buoyantly neutral fluorescent tracers with a diameter of  $0.92 \mu\text{m}$  (Fluoresbrite Multifluorescent from Polysciences). A series of 1000 flow images was acquired corresponding to each value of the flow rate  $Q$  with a digital camera. The images were acquired at the midplane of the microchannel and at middistance downstream. For the experiments in which the flow rate did not exceed  $10 \mu\text{L}/\text{min}$ , we have used a Prosilica GE camera with 16-bit quantization (model GE680C from Allied Technologies). The maximal frame rate achievable with this camera is 200 fps. During the experiments with flow rates  $Q \in [10, 23] \mu\text{L}/\text{min}$ , a Mikrottron camera has been used up to a frame rate of 500 fps.

### C. Data analysis

The main tool used to systematically characterize the microscopic flow was adaptive multigrid digital particle image velocimetry (DPIV) (see Refs. [45,46] for a detailed description of the method) entirely developed in-house under MATLAB (together with the “Image Processing Toolbox”), which followed the steps briefly described below. The first step of the data acquisition procedure was to precisely identify the borders of the microchannel. Though apparently trivial, this step is crucial for correctly measuring the slip velocity and the wall velocity gradients, which represent the core of the present study. To do so, we have built from the entire sequence of acquired images a space-time diagram  $xt = xt(t, y)$  of the transversal (to the flow direction) profiles of image brightness acquired at the middle of the field of view [Fig. 4(a)]. Next, we have computed the root mean square deviation (rmsd) of the space-time diagram along its temporal axis according to

$$I^{\text{rms}}(y) = (\langle [xt(t, y) - \langle xt(t, y) \rangle_t]^2 \rangle_t)^{1/2}. \quad (1)$$

Here  $\langle \cdot \rangle_t$  denotes the average of a two-dimensional array computed along its temporal dimension  $t$ . Lastly, we identify the edges of the channel by finding the two local maxima of the dependence  $|dI^{\text{rms}}(y)/dy|$  represented in Fig. 4(b) by the circles.

Second, a background was calculated by averaging all the images of the first time series we have acquired. Third, the average background was subtracted from the images. Finally, pairs of preprocessed images separated in time by the interframe  $t_1$  are passed to a multipass DPIV algorithm using a sequence of squared interrogation windows with sizes [128, 64, 32, 16, 8]. As a postprocessing step, each computed velocity field obtained from the DPIV algorithm was filtered using a median filter. The spatial resolution of the velocity fields was  $4.5 \mu\text{m}$  (44 times smaller

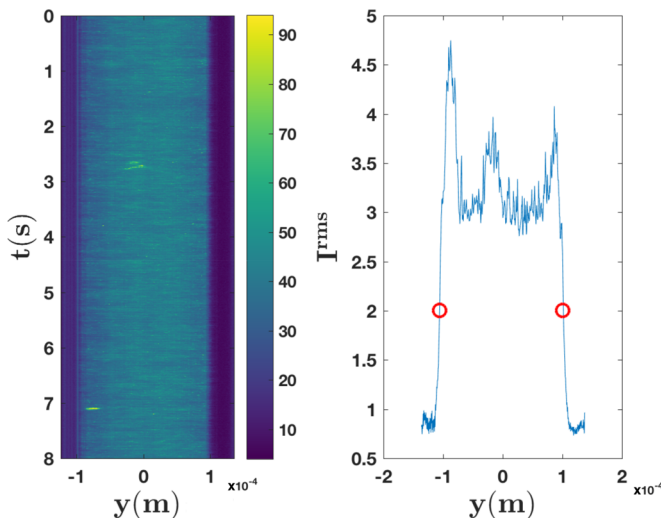


FIG. 4. The plot on the left refers to the space-time of the transversal profiles of image brightness acquired at the middle of the field of view. The plot on the right refers to the root mean square deviation (rms) of the brightness of the space-time diagram along the temporal direction.

than the width of the channel), which suffices for a reliable calculation of the velocity gradients in proximity to the channel walls. Corresponding to each driving flow rate, we have computed the average of 1000 subsequent velocity fields together with their root mean square deviation (rms), which allowed one to specify error bars. To compute accurately the velocity gradients, each profile of the time-averaged velocity was first fitted by a smoothing spline function, which was differentiated analytically in order to avoid the inherent errors associated with the classical numerical differentiation.

To extract the wall slip velocity, we have extrapolated each spline fitting function of the axial velocity and computed its value at the level of the wall. The velocity gradient near the wall was assessed via the slope of the last four points of the smoothing spline function. The size of the rigid plug located along the center-line of the microchannel was estimated by detecting the position where the transversal gradient of the axial velocity becomes larger than 0.3% of its maximal value along the velocity profile. The plug velocity was calculated by averaging the velocity within the plug region.

## II. RESULTS

### A. Description of the flow regimes in the presence of wall slip

We focus in the following on the experimental characterization of the microscopic flow profiles of a Carbopol gel in a steady channel flow for several flow rates. Profiles of the time-averaged flow velocity  $U_{av}$  measured according to the method described in Sec. I C are presented in Fig. 5. Due to the axial symmetry of the flow, velocity profiles were plotted only across the half-width of the channel ( $y = 0$  corresponds to the center-line of the microchannel and  $y = 1 \times 10^{-4}$  m corresponds to the channel wall). The standard deviation of the velocity profiles was smaller than 5% for different values of flow rates. Depending on the magnitude of the constant imposed flow rate  $Q$ , three distinct flow regimes are observed in Fig. 5.

At low driving flow rates ( $Q < 2 \mu\text{L}/\text{min}$ ), a full plug flow regime is observed in Fig. 5(a). The entire Carbopol gel is unyielded and, according to some authors (e.g., see Refs. [34,47]), it “slides” over a very thin liquid layer located in proximity to the channel walls. We once more emphasize, however, that this simple phenomenological picture has not yet been confirmed by

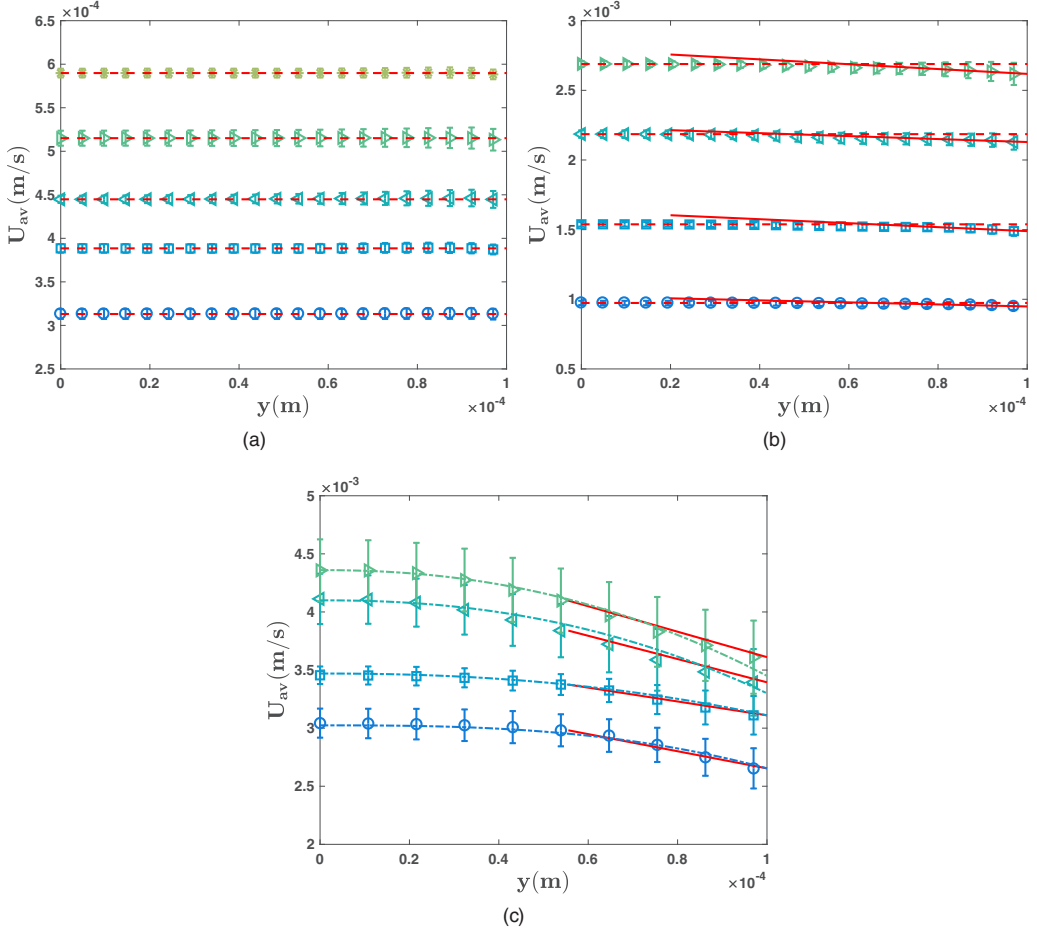


FIG. 5. Velocity profiles for different values of flow rate  $Q$ . Panel (a) corresponds to the solid regime: circles,  $Q = 1 \mu\text{L}/\text{min}$ ; squares,  $Q = 1.4 \mu\text{L}/\text{min}$ ; left triangles,  $Q = 1.6 \mu\text{L}/\text{min}$ ; right triangles,  $Q = 1.8 \mu\text{L}/\text{min}$ ; stars,  $Q = 2 \mu\text{L}/\text{min}$ . Panel (b) corresponds to the transition: circles,  $Q = 3.5 \mu\text{L}/\text{min}$ ; squares,  $Q = 5.5 \mu\text{L}/\text{min}$ ; left triangles,  $Q = 8 \mu\text{L}/\text{min}$ ; right triangles,  $Q = 10 \mu\text{L}/\text{min}$ . Panel (c) corresponds to the fluid regime: circles,  $Q = 14 \mu\text{L}/\text{min}$ ; squares,  $Q = 15 \mu\text{L}/\text{min}$ ; left triangles,  $Q = 21 \mu\text{L}/\text{min}$ ; right triangles,  $Q = 23 \mu\text{L}/\text{min}$ . The dash-dotted lines are fitting functions according to the analytical solution of the Poiseuille flow of a power-law fluid given by Eq. (2). To better visualize the plug region, dashed horizontal lines are plotted in panels (a), (b).

direct visualization of the solid material units during the flow. The full plug velocity profiles are characteristic of a solidlike behavior visible in Fig. 1 [region (S)] and phenomenologically consistent with the observations of Pérez-González *et al.* [15].

As the flow rate is gradually increased past this first flow regime, a second flow regime is observed. The Carbopol gel is partially yielded in proximity to the channel walls (where the velocity gradients are the largest), but a central unyielded plug may still be observed around the center-line of the microchannel [Fig. 5(b)]. The shear stresses are not large enough to yield the material along the entire width of the channel. This behavior might be related to the solid-fluid transition ( $S + F$ ) of the material observed in Fig. 1, where the solid and fluid material elements coexist.

As the flow rate is increased even further ( $Q > 10 \mu\text{L}/\text{min}$ ), the Carbopol gel is fully yielded across the entire width of the channel in the sense that the central plug becomes negligibly narrow,

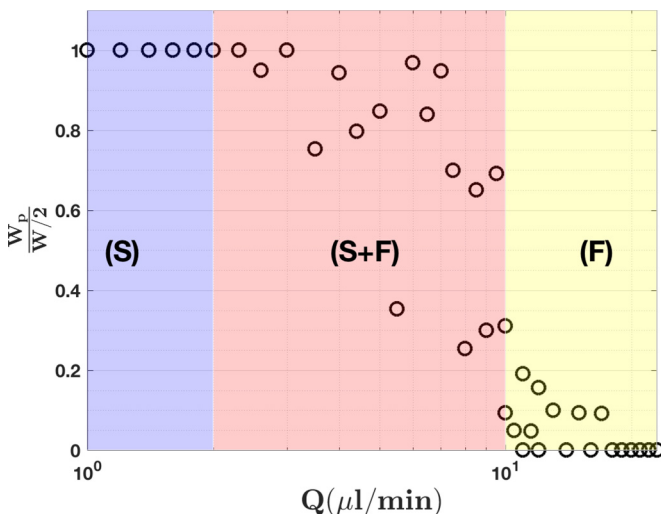


FIG. 6. Dependence of the normalized plug width  $2W_p/W$  on the applied flow rate  $Q$ . The symbols marking the highlighted regions denote the deformation regimes and are explained in the text: (S), solid; (S + F), solid-fluid coexistence; (F), fluid.

which is a qualitative indicator that this flow regime corresponds to the fluid rheological regime (F) observed in Fig. 1.

As a more quantitative argument, we note that the velocity profiles presented in Fig. 5(c) may be well fitted by the analytical solution of the Poiseuille flow of power-law fluid [48]:

$$U_{av} = U_s + C \left[ 1 - \left( \frac{2y}{W} \right)^{1+\frac{1}{n}} \right], \quad (2)$$

where the prefactor  $C$  is a fit parameter and  $n \approx 0.64$  is the power-law index of the Carbopol gel obtained via a Herschel-Bulkley fit (see Fig. 1).

Corresponding to each flow regime, the velocity profiles clearly exhibit a slip behavior at the channel walls (a nonzero slip velocity at  $y = 1 \times 10^{-4}$  m). The measured slip velocity is systematically larger than the error bar of the velocity profile near the wall.

The measured velocity profiles allow one to compute the velocity gradients near the wall, the slip, and plug velocities and the plug size  $W_p$  defined by the extent of the flat central region. The evolution of the size of the rigid plug  $W_p$  with the flow rate is presented in Fig. 6. At low values of flow rate ( $Q < 2 \mu\text{L}/\text{min}$ ), the plug size is practically independent of the flow rate: the plug fills the entire width of the channel. Beyond ( $Q \approx 2 \mu\text{L}/\text{min}$ ) the plug size decreases as  $Q$  is increased. The shear stresses are not large enough to yield the material along the entire width of the microchannel. Beyond a critical value of the flow rate ( $Q > 10 \mu\text{L}/\text{min}$ ), a plug is no longer observed ( $W_p \approx 0$ ) and the material becomes fully yielded. In this case, the local shear stresses exceed the yield stress nearly everywhere across the channel width except (perhaps) for a narrow region centered around the local maximum of the velocity profile, which cannot be resolved by our measurements.

### B. Scaling behavior at the wall within various flow regimes

As already emphasized in the Introduction, understanding the scaling behavior of the relevant hydrodynamic quantities (shear stress, shear rate, slip velocity) in proximity to the wall is of paramount importance to developing reliable microscopic models that can explain the confined flows of viscoplastic materials in the presence of wall slip and for the implementation of numerical

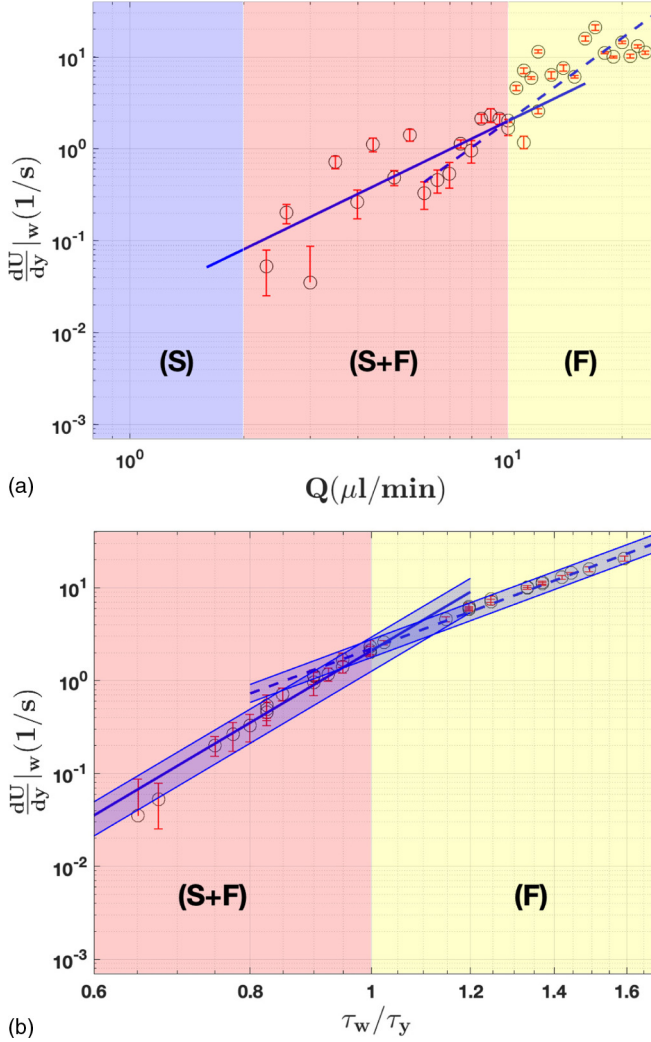


FIG. 7. (a) Dependence of the wall velocity gradient on the applied flow rate  $Q$ . The solid line and the dashed line are guides for the eye,  $\frac{dU}{dy}|_w \propto Q^2$  and  $\frac{dU}{dy}|_w \propto Q^3$ , respectively. (b) Dependence of the wall velocity gradient on the reduced wall shear stress  $\tau_w/\tau_y$  computed using the rheological measurements and computed wall velocity gradients. The solid line and the dashed line are power-law fitting functions,  $\frac{dU}{dy}|_w \propto \tau_w^{8 \pm 0.5}$  and  $\frac{dU}{dy}|_w \propto \tau_w^{5 \pm 0.3}$ , respectively. The blue shaded regions overlapping onto the fit functions represent the error bounds of the power-law fitting functions.

simulations. Based on the characterization of the flow fields presented in Sec. II A, we study in this section the scaling behavior for each flow regime previously identified.

The dependence of the wall velocity gradients computed according to the procedure detailed in Sec. I C on the flow rate  $Q$  is presented in Fig. 7(a). As the fair amount of scatter of the data prevented us from reliably performing a power-law fit, the full and dashed lines are only guides for the eye. In the solid region (S), the material is fully unyielded and, within the instrumental accuracy of our technique, no velocity gradients could be reliably measured near the solid wall. As the flow rate  $Q$  is gradually increased, one can clearly notice the existence of two different scaling regimes. Within the solid-fluid transition regime (S + F), the wall velocity gradient scales with the flow rate

as  $\frac{dU}{dy}|_w \propto Q^2$  [see the full line in Fig. 7(a)]. A further increase of the flow rate into the fluid regime ( $F$ ) leads to a different scaling of the wall velocity gradient,  $\frac{dU}{dy}|_w \propto Q^3$  [see the dashed line in Fig. 7(a)].

The measurements of the wall velocity gradients  $\frac{dU}{dy}|_w$  allow one to compute the wall shear stresses  $\tau_w$  using the macrorheological measurements presented in Fig. 1. To do so, we interpreted  $\frac{dU}{dy}|_w$  as the relevant scale for the rate of shear, and we interpolated the corresponding stress from the macrorheological flow curve presented in Fig. 1. The result of this evaluation is presented in Fig. 7(b). Two different scaling regimes of the wall shear rate with the wall shear stress can be clearly observed. The first scaling regime corresponds to a partial yielding of the gel in the vicinity of the wall,  $\frac{dU}{dy}|_w \propto \tau_w^{8 \pm 0.5}$  [see solid line in Fig. 7(b)]. Above a critical value of wall shear stress and corresponding to the fluid deformation regime, a second scaling regime is observed,  $\frac{dU}{dy}|_w \propto \tau_w^{5 \pm 0.3}$  [see the dashed line in Fig. 7(b)]. The blue shaded regions overlapping onto the power laws indicate the error bounds of the power-law fitting functions.

The data presented in Fig. 7(b) prompt us to revisit the dependence of the plug size  $W_p$  presented in Fig. 6. According to Fig. 7(b), the maximum value of the wall shear stress is  $\tau_w^{\max} \approx 1.8\tau_y$ . If the microscopic flow was accurately described by the Herschel-Bulkley analytical solution (for the analytical solution, we refer the reader to Ref. [49]), then the minimum size of the solid plug  $W_p$  corresponding to the maximum wall shear stress  $\tau_w^{\max}$  should be  $W_p = \frac{\tau_y}{\tau_w^{\max}} W \approx 0.55 W$ . As the instrumental resolution of the plug measurements presented in Fig. 6 would certainly allow the detection of such a value, we can only conclude at this point that the theoretical prediction for the plug width based on the Herschel-Bulkley law does not work in this case. This conclusion corroborates well with the lack of applicability of the Herschel-Bulkley model in describing confined microscopic flows of a Carbopol gel discussed in Refs. [18,19].

The scaling exponent obtained by fitting the data corresponding to the fully yielded regime differs from the power-law exponent obtained by the Herschel-Bulkley fitting to the macro-rheological measurements. This difference might be attributed as well to the confinement [18,19]. However, we can notice that the value of the critical wall shear stress defined as the intersection between the two power laws is close to the yield stress measured in the rheometric flow and fitted by the Herschel-Bulkley model (see Fig. 1).

The dependence of the slip velocity  $U_s$  on the wall shear stress  $\tau_w$  is presented in Fig. 8(a). Because in the solid regime the wall velocity gradients are too small to be reliably measured, we could not use the method described above to reliably compute the wall shear stresses. For higher flow rates [beyond the ( $S$ ) regime], again, two distinct scaling laws are observed. Corresponding to the solid-fluid coexistence regime ( $S + F$ ),  $U_s \propto \tau_w^{3.5}$ . Within the fully yielded regime ( $F$ ),  $U_s \propto \tau_w$ .

The dependence of the slip velocity  $U_s$  on the wall velocity gradients  $\frac{dU}{dy}|_w$  is illustrated in Fig. 8(b). Within the ( $S + F$ ) and ( $F$ ),  $\frac{dU}{dy}|_w$  scales as  $U_s \propto (\frac{dU}{dy}|_w)^{0.5}$  and  $U_s \propto (\frac{dU}{dy}|_w)^{0.2}$ , respectively.

### C. Comparison with previous results from the literature

We compare in the following the scaling laws described in Sec. II with results obtained by others. Pérez-González *et al.* have investigated the scaling behavior in a millimeter-sized glass channel [15]. They have estimated the apparent shear rate  $\dot{\gamma}_a$  and the wall shear stress  $\tau_w$  as  $\dot{\gamma}_a = \frac{32Q}{\pi D^3}$  and  $\tau_w = \frac{\Delta P}{4\frac{L}{D}}$ , respectively, where  $\Delta P$  is the pressure drop between the capillary ends,  $L$  and  $D$  are, respectively, the length and the diameter of the borosilicate glass capillary, and  $Q$  is the flow rate calculated from the integration of the velocity profiles. Consistent with our findings, they identify three distinct flow regimes: a purely plug flow before yielding, solid-liquid transition, and shear thinning at relatively high shear rates. The apparent shear rate  $\dot{\gamma}_a$  scales with the wall shear stress  $\tau_w$  as  $\dot{\gamma}_a \propto \tau_w^{2.5}$  in the fluid regime. This scaling law differs significantly from the one we observe,

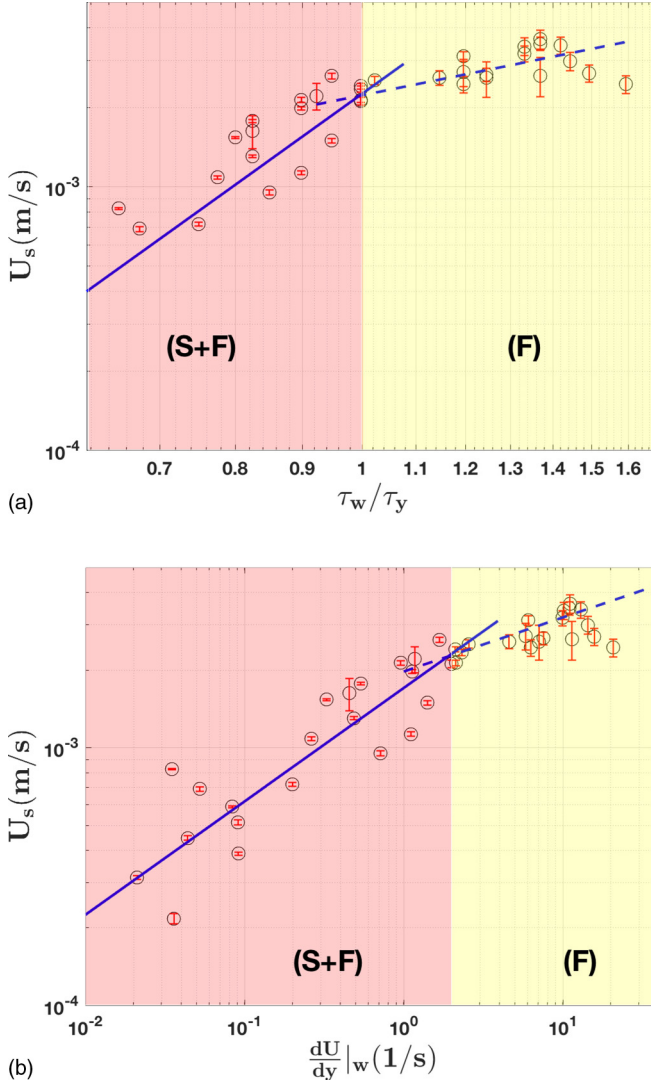


FIG. 8. (a) Dependence of the wall slip velocity  $U_s$  on the wall shear stress  $\tau_w$ . The full (—) and dashed (---) lines are guides for the eye,  $U_s \propto \tau_w^{3.5}$ ,  $U_s \propto \tau_w$ , respectively. (b) Dependence of the wall slip velocity  $U_s$  on the wall velocity gradient  $\frac{dU}{dy}|_w$ . The full and dashed lines are guides for the eye,  $U_s \propto (\frac{dU}{dy}|_w)^{0.5}$  and  $U_s \propto (\frac{dU}{dy}|_w)^{0.1}$ , respectively. The symbols marking the highlighted regions denote the deformation regimes and are explained in the text: (S + F), solid-fluid coexistence; (F), fluid.

$\frac{dU}{dy}|_w \propto \tau_w^5$  [the dashed line in Fig. 7(b)]. This difference might be related to the way  $\dot{\gamma}_a$  is calculated ( $\dot{\gamma}_a = \frac{32Q}{\pi D^3}$ ). This formula assumes that the velocity profile is parabolic and there exists no velocity slip at the walls, which, obviously, is not the case for a Carbopol gel flowing in a glass capillary.

By direct observation of a rheometric flow of a microgel, Meeker *et al.* in Ref. [50] observe that  $U_s$  remains constant for  $1 < \frac{\tau}{\tau_y} < 1.5$  while in our experiments the slip velocity increases linearly with the wall shear stress,  $U_s \propto \tau_w$ .

The same authors observe in a subsequent publication three slip regimes in a macrorheological setup [7]. In a solid regime, they find a slip velocity that scales as the stress squared, whereas in the

intermediate deformation regime they find a constant slip velocity. These scaling results are obtained within the framework of a phenomenological microelastohydrodynamic lubrication. As we use no model for assessing the scaling behavior, a comparison is rather difficult to make.

Péméja and co-workers have obtained two wall slip scaling laws for the microchannel flow of a Carbopol gel: for low wall shear stresses,  $\tau_w < 100$  Pa  $U_s \propto \tau_w^2$ , whereas for higher stresses they obtain a linear scaling. The quadratic scaling law is at odds with the result presented in Fig. 8(a),  $U_s \propto \tau_w^{3.5}$ , whereas the linear scaling law is consistent with our findings. This partial agreement may be explained by the way Péméja compute the wall shear stress using the driving pressure drop  $\Delta p$ ,  $\tau_w = \frac{h}{2L} \Delta p$  ( $L$  being the length of their microchannel and  $h$  its depth). This correlation may become relatively accurate “only” far from the yield point, whereas it is most probably formal in the solid ( $S$ ) and in the intermediate ( $S + F$ ) regimes.

To describe the wall slip behavior, Kaylon proposed the following relationship between the slip velocity and the wall shear stress [16]:

$$U_s = \beta(\tau_w)^{1/n_b}. \quad (3)$$

Here  $\beta$  relates the width of the slip layer  $\delta$  to the consistency of the binder fluid  $m_b$  and to its power-law index  $n_b$ ,  $\beta = \frac{\delta}{m_b^{1/n_b}}$ . This simple phenomenological scaling relationship is derived based on the assumption of the existence of a depleted layer of solvent of width  $\delta$  in proximity to the solid boundary (such an assumption is often used in order to derive simple phenomenological scaling models; see, e.g., Ref. [11]). The Carbopol gel is considered as a jammed system of swollen gel microparticles [34]. As the solvent of the Carbopol gel was deionized water, the “binder fluid” might be considered as Newtonian,  $K_b = 10^{-3}$  Pa s and  $n_b = 1$ .

In the fluid regime,  $U_s$  scales linearly with  $\tau_w$ ,  $U_s \propto \tau_w$  [the dashed line in Fig. 8(a)]. The full/dashed lines are guides for the eye. This linear scaling law confirms the assumption that the “binder fluid” is Newtonian,  $n_b = 1$ . A similar scaling law was found by Poumaere *et al.* [14] while it differs from the ones predicted theoretically by Piau [34]:  $U_s \propto \tau_w^{1/3}$  for a loosely packed system and  $U_s \propto \tau_w^2$  for a closely packed system. This difference might be related to the fact that the lubricating fluid is considered to be non-Newtonian fluid in Ref. [34].

In our study, the measured factor  $\beta = 70 \times 10^{-6}$  m Pa $^{-1}$  s $^{-1}$  leads to a slip layer of thickness  $\delta \approx 0.07$   $\mu$ m. This value is of the same order of magnitude as the one found by Jiang *et al.* [51],  $\delta \approx 0.1$   $\mu$ m, and by Poumaere *et al.* [14],  $\delta \approx 0.23$   $\mu$ m. However, this width obtained by such simple estimates is far too small to be accessible via direct visualization of the flow, meaning that the main hypothesis used to predict this scaling remains for now just a hypothesis. This once more justifies our approach of relying on no assumption but computing the stresses by relating the steady-state rheological behavior to the *in situ* measurements of the wall velocity gradients.

The dependence of the slip velocity on the wall velocity gradient is presented in Fig. 8(b). Once more, due to the rather large scatter of the data, the full/dashed lines are just guides for the eye. Within the  $S + F$  regime we observe a dependence  $U_s \propto (\frac{dU}{dy}|_w)^{0.5}$  whereas in the fluid regime ( $F$ ) the scaling behavior changes to  $U_s \propto (\frac{dU}{dy}|_w)^{0.2}$ .

### III. ON THE POSSIBILITY OF INHIBITING THE WALL SLIP IN AN ACRYLIC-MADE MICROCHANNEL

There exist a number of situations when the emergence of the wall slip phenomenon may turn quite problematic. The best known example relates, perhaps, to the macrorheological characterization of pasty materials where the presence of walls leads to systematic errors, particularly around the yield point. From a theoretical and numerical perspective, the presence of wall slip is equally troublesome as, to the best of our knowledge, there exists no fundamental theory that rigorously captures the scaling behavior of the slip velocity at the wall, and the choice of a slip law is often arbitrary. A direct way of eliminating the wall slip, which is commonly used during macrorheological tests performed with pasty materials, is to use mechanically rough solid surfaces.

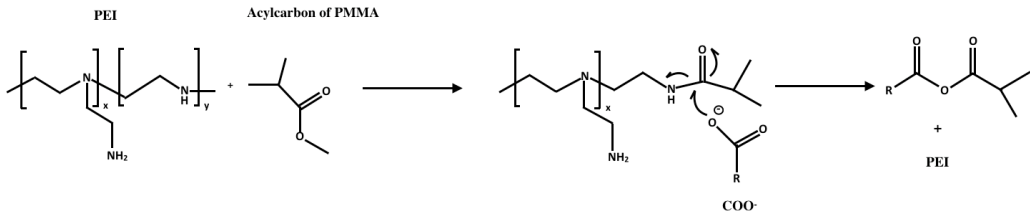


FIG. 9. Chemical reaction leading to the attachment of the Carbopol gel on the PMMA surface.

Though effective in eliminating the wall slip, this solution comes at a price difficult to cope with during experiments that require the *in situ* visualization of the flow structure, namely the loss of the optical transparency. An alternative method relates to “*engineering*” a special chemical treatment that facilitates the adhesion of the microstructural elements of the pasty material to a solid wall without altering its optical transparency. For the case of a Carbopol gel, Metivier and co-workers proposed a chemical reaction that can eliminate the slip along a smooth acrylic-made wall [53]. The authors of this study prove the effectiveness of their method via macrorheological tests performed with various gaps and indicate and equally emphasize its temporal stability over the course of 46 days. A detailed investigation of the physical mechanisms responsible for the apparent macroscopic effectiveness of this solution is, however, missing. After providing a detailed description of the chemical reaction, we focus in the following on a detailed analysis of this solution via both macrorheological tests and microfluidic experiments.

#### A. Chemical treatment of the microchannel

The solution proposed by Metivier and her co-workers consists of depositing a thin layer of polyethylenimine PEI (Aldrich) on the Polymethyl methacrylate *PMMA* surface. Low concentrations of PEI solutions with concentrations  $C$  ranging in between  $10^{-8}$  % (wt) and 2% (wt) at neutral pH have been prepared by dissolving the right amount of PEI in deionized water. The PMMA substrate was immersed into the PEI polymer solution during times ranging between 60 s and 24 h, and the final results are unchanged. Finally, they have soaked the chemically treated substrate into double deionized water for 6 h in order to remove the excess (unreacted) of PEI.

The idea of the chemical treatment first proposed by Metivier and her co-workers actually originates from a previous study by Kitagawa *et al.* [52]. Though apparently similar, the exact details of the procedure of Kitagawa *et al.* are actually quite different. The PMMA microchip was cleaned by damping it in methanol for 10 min and then rinsing in deionized water. A significantly higher concentration of PEI solution  $C = 10\text{--}20$  wt. % was used. To neutralize the PEI solutions, a borate buffer was equally added to the mixture. The neutralized solution was continuously circulated through the microchannel for 2 h. The microchannel was rinsed in deionized water for another 20 min.

As only Metivier and her co-workers have studied the influence of the chemical treatment on the wall slip of Carbopol in Ref. [53], we have decided in our study to follow their procedure rather than that of Kitagawa *et al.* We used PEI solutions of 0.5 wt. % concentration. We found that the pH is not neutral even for low concentration of PEI,  $\text{pH} \approx 10.7$ . The immersing time of our PMMA substrates was for 24 h.

According to Refs. [52,53], the idea of these methods relies on a chemical reaction between the acylcarbon groups (ester groups) of the PMMA substrate with the secondary amino groups of PEI and a reaction between the  $\text{COO}^-$  groups of the Carbopol gel with the amino groups of PEI [53]. After a closer analysis of the chemical reaction in terms of the chemical affinity of the reactants, we conclude that the  $\text{COO}^-$  groups of the Carbopol gel actually bind to the amido groups, as shown in Fig. 9.

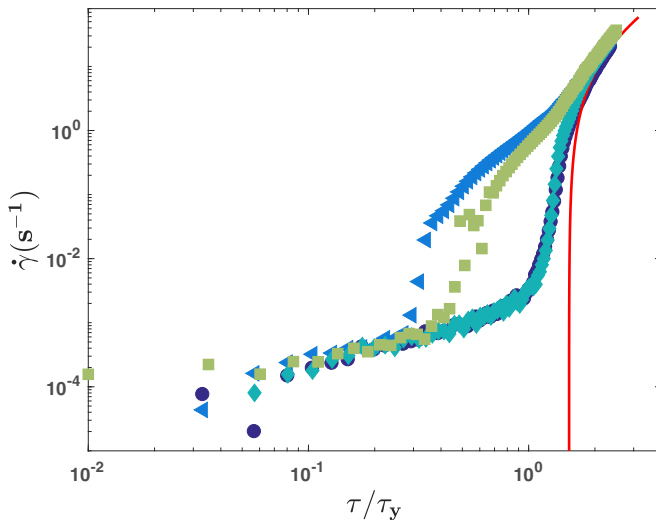


FIG. 10. Macrorheological measurements of the dependence of the rate of deformation  $\dot{\gamma}$  on the reduced applied stress for various slip conditions on the bottom plate: circles, no slip (glass paper glued on the bottom plate); diamonds, chemically treated acrylic block used as a bottom plate immediately after the chemical treatment was completed; squares, chemically treated acrylic block used as a bottom plate one week after the chemical treatment; triangles, untreated acrylic block used as a bottom plate. The full line is a fit according to the Herschel-Bulkley model.

These bonds lead to the attachment of Carbopol microgel particles to the PMMA substrate and the formation of a Carbopol layer that is essential in preventing the wall slip. We also note that, according to Fig. 9, some PEI molecules remain in the solution.

### B. Assessment of wall slip behavior via macrorheological measurements

First, we have assessed the effectiveness of the chemical treatment by means of macrorheological tests. For this purpose, we have machined two identical acrylic blocks and treated only one of them according to the protocol described in Sec. III A while leaving the second chemically unaltered. The acrylic blocks have been used as bottom plates for macrorheological tests. We note that the macrorheological experiments with the chemically treated acrylic block were performed immediately after the treatment was completed, thus avoiding any degradation of the chemical treatment in time. The temporal stability of the treatment will be discussed separately in Sec. III C. For all the experiments we have performed, glass paper was glued on the top plate (as described in Sec. IA 2). Thus, the wall slip might solely occur on the bottom plate. The results of this comparative macrorheological investigation are summarized in Fig. 10, which presents the dependence of the measured rate of deformation  $\dot{\gamma}$  on the reduced applied stress  $\tau/\tau_y$  for several slip conditions on the bottom plate. When a chemically treated acrylic block is used as a bottom plate (the diamonds in Fig. 10), the macrorheological measurements are practically identical to those performed in the absence of wall slip (when both plates are covered with glass paper; see the circles in Fig. 10). On the other hand, the measurements performed with the untreated acrylic block as a bottom plate (the triangles in Fig. 10) deviate strongly from the measurements performed in the absence of slip, particularly around the yield point,  $\frac{\tau}{\tau_y} \approx 1$ . To conclude this part, from a macrorheological perspective, the wall slip effects are negligible when the acrylic surfaces of the rheometric geometry are chemically treated, and the rheological tests are conducted immediately after the treatment.

This conclusion is in general agreement with the main point made in Ref. [53]. To this end, however, the microscopic physical mechanism behind the apparent macroscopic effectiveness of

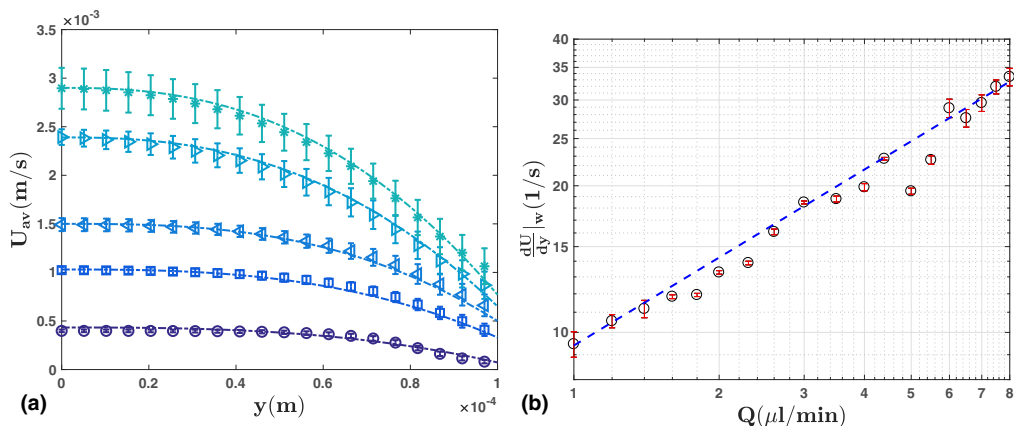


FIG. 11. (a) Velocity profiles measured in the chemically treated microchannel at various flow rates: circles,  $Q = 1 \mu\text{L}/\text{min}$ ; squares,  $Q = 2.6 \mu\text{L}/\text{min}$ ; left triangles,  $Q = 4 \mu\text{L}/\text{min}$ ; right triangles,  $Q = 6.5 \mu\text{L}/\text{min}$ ; stars,  $Q = 8 \mu\text{L}/\text{min}$ . The dash-dotted lines are fitting functions according to analytical solution of the Poiseuille flow of a power-law fluid given by Eq. (2). (b) Dependence of the wall velocity gradients measured in the chemically treated microchannel on the applied flow rate  $Q$ . The dashed line (--) is a guide for the eye,  $\frac{dU}{dy}|_w \propto Q^{0.6}$ .

this chemical treatment remains elusive. To gain further insights into this, we focus in the upcoming section on a detailed characterization of flows in chemically treated microchannels and on their comparison with the flows in the presence of wall slip described in Sec. II.

### C. Slip behavior in chemically treated microchannels

To understand the impact of the chemical treatment on the microscopic flows, we have performed measurements similar to those performed in the presence of wall slip with chemically treated microchannels. The operating flow rates were chosen in the same range as in the case of the experiments described in Sec. II.

Velocity profiles measured in the chemically treated microchannel for several flow rates are presented in Fig. 11(a). Unlike in the case of the untreated channels, we no longer observe either a full plug flow regime as illustrated in Fig. 5(a) or an intermediate regime as in Fig. 5(b). For each flow rate  $Q$ , the velocity profiles are qualitatively similar to those observed in the yielded regime illustrated in Fig. 5(c), and they can be fitted by the analytical solution for the Poiseuille flow of a power-law fluid given by Eq. (2).

A direct consequence of the chemical treatment relates to larger velocity gradients in proximity to the wall as well as to smaller slip velocities, as visible in Fig. 11(b). However, these measurements clearly indicate that the slip at the wall is not completely removed by the chemical treatment but only inhibited. Thus, at a microscopic scale, the effectiveness of the chemical treatment is only partial.

The comparison of the dependencies of the plug velocity  $U_p$ , slip velocity  $U_s$ , and the wall shear rates  $\frac{dU}{dy}|_w$  on the driving flow rate  $Q$  measured in chemically treated and untreated channels is shown in Fig. 12. As already noted, for the case of the chemically treated channel, the slip velocity is smaller than in the case of the untreated channel [Fig. 12(a)]. Consequently, the plug velocity is systematically larger in the treated channel.

The dependence of the wall velocity gradients on the wall shear stress measured in the chemically treated channel is fully consistent with the measurements performed with the untreated channel in the third flow regime [Fig. 12(c)]. This reinforces the statement that in the chemically treated

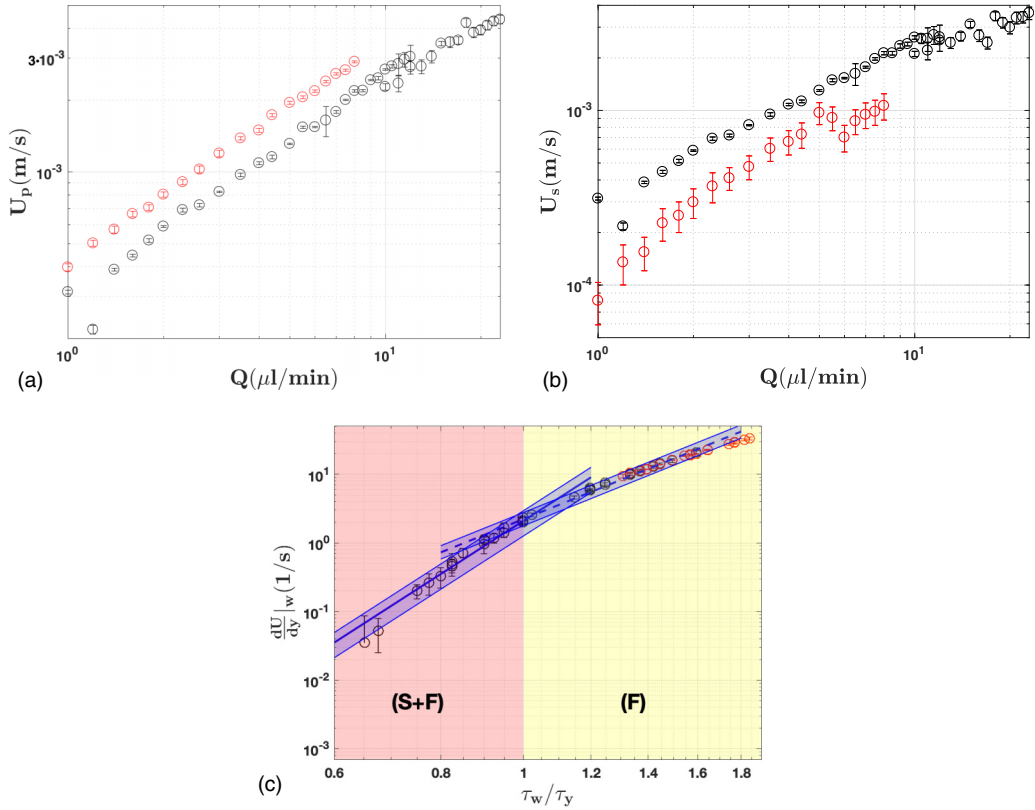


FIG. 12. (a) Dependence of the slip velocity  $U_s$  on the volumetric flow rate  $Q$ . (b) Dependence of the plug velocity  $U_p$  on the volumetric flow rate  $Q$ . (c) Dependence of the wall velocity gradient  $\frac{dU}{dy}|_w$  vs wall shear stress  $\tau_w$ . Black/red circles correspond to the treated/untreated PMMA microchannel. The blue shaded regions overlapping onto the fit functions represent the error bounds of the power-law fits.

channel, a single flow regime is observed corresponding to the largest flow rates investigated with the untreated channel.

To gain further insights into the physical mechanism by which the chemical treatment affects the slip behavior, we turn our attention to the direct visualization of the flow in both untreated

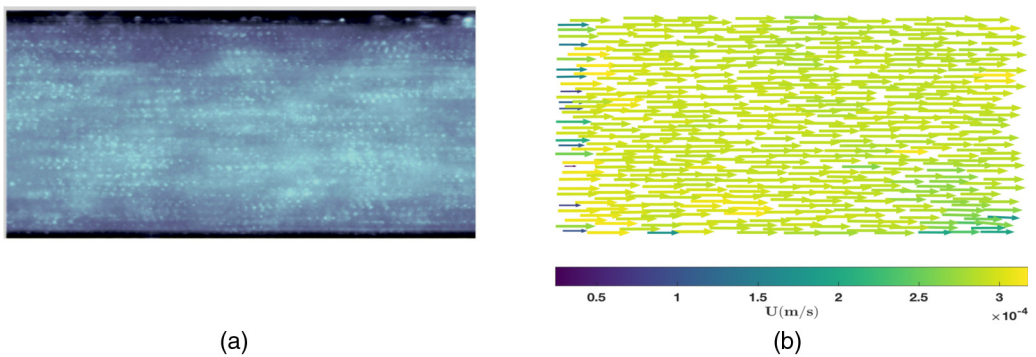


FIG. 13. (a) Streak imaging of the flow in the untreated microchannel. (b) Velocity field measured in the chemically untreated channel. The flow rate was  $Q = 1 \mu\text{L}/\text{min}$ .

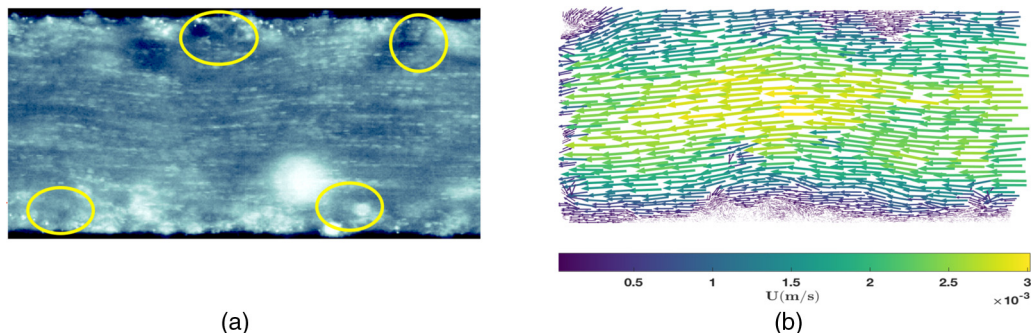


FIG. 14. (a) Streak imaging of the flow in the chemically treated microchannel. The yellow ellipses highlight blobs of the gel rigidly attached to the walls. (b) Velocity field measured in the chemically treated channel. The flow rate was  $Q = 1 \mu\text{L}/\text{min}$ .

and chemically treated channels at the same flow rate  $Q = 1 \mu\text{L}/\text{min}$ . Two distinct methods of flow visualization have been employed. First, we have performed direct imaging of the streaks of the micro-PIV seeding particles by overexposing the images prior to acquisition. This kind of visualization offers primary insights into the structure of the microscopic flow. Second, we display the corresponding microscopic flow fields.

The flow in the untreated channel is described in Fig. 13. As one would expect for the case of a steady and laminar flow, the streak lines are rectilinear and parallel to the walls of the micro-channel [Fig. 13(a)]. Consequently, the velocity field exhibits no component in the direction transversal to the flow [Fig. 13(b)].

The flow in the chemically treated microchannel is illustrated in Fig. 14. The image of the streaks of the seeding particles reveal the presence of rigid blobs of Carbopol unevenly attached to the walls of the microchannel [the regions highlighted by the yellow ellipses in Fig. 14(a)]. By monitoring the streak line behavior at various positions downstream, we have observed no regularity of their distribution along the channel walls and thus we have concluded that their appearance is rather random. We attribute this apparent randomness to the polydispersity of the Carbopol microstructure, which has been demonstrated experimentally [40,54]. The presence of these solid blobs attached to the microchannel walls triggers a secondary flow [Fig. 14(b)]. Whereas in a macroscopic geometry this effect might be of little or no importance, in a microchannel with a size of the same order of magnitude as the average size of the gel particles this effect can no longer be ignored.

A second issue related to the overall effectiveness of this chemical treatment is its temporal stability. To address this issue, we have performed macrorheological tests similar to those presented in Fig. 10 after keeping the chemically treated acrylic blocks in a beaker filled with deionized water for one week in conditions of gentle stirring with a magnetic stirring rod. The result was that the slip behavior illustrated in Fig. 10 was restored, which indicated that the effectiveness of the treatment was basically lost (squares in Fig. 10).

#### IV. SUMMARY OF CONCLUSIONS, OUTLOOK

An experimental investigation of the wall slip phenomenon during a steady microflow of a Carbopol gel was carried out in this study. By means of digital particle image velocimetry, accurate measurements of the flow fields have been performed in a wide range of flow rates. Depending on the magnitude of the flow rate, three distinct flow regimes are observed. At low driving flow rates, a full plug flow regime is observed [Fig. 5(a)]. The full plug flow regime may be understood in terms of a solid body of unyielded gel sliding over a thin layer of depleted solvent expelled from the spongy Carbopol structural units in the vicinity of the solid walls. As the flow rate is gradually increased, the Carbopol gel is partially yielded in the proximity of the channel walls, but a central

unyielded plug may still be observed around the center-line of the microchannel [Fig. 5(b)]. As the flow rate is increased even further, the Carbopol gel is fully yielded across the entire width of the channel [Fig. 5(c)].

As the flow rate is increased past the full plug regime, the plug length  $W_p$  decreases monotonically from a value equal to the half channel width  $W/2$  to zero (Fig. 6). The scaling behavior of the wall velocity gradients  $\frac{dU}{dy}|_w$  with the flow rate is illustrated in Fig. 7(a). Within the partially yielded regime,  $\frac{dU}{dy}|_w \propto Q^2$ , whereas within the fully yielded regime,  $\frac{dU}{dy}|_w \propto Q^3$ .

Measurements of the velocity profiles allow one to obtain the wall velocity gradients and slip velocities by extrapolating the velocity profiles at the channel walls. We use the dependence between the stress and the rate of shear obtained via classical rotational rheometry, and we relate the measured wall velocity gradients to the wall stresses in order to obtain experimentally the scaling laws for the wall slip phenomenon.

As compared to a number of previous studies that inferred the wall velocity gradients and the wall shear stresses directly from the driving pressure drops and flow rates [15,19,21], this procedure has the important advantage of making absolutely no assumption on either the flow structure or the rheological behavior of the material. The scaling behavior of the wall velocity gradients with respect to the wall shear stresses is illustrated in Fig. 7(b). Within the partially yielded regime, the wall velocity gradients scale as  $\frac{dU}{dy}|_w \propto \tau_w^{7.99}$ , whereas in the fully yielded regime they scale as  $\frac{dU}{dy}|_w \propto \tau_w^{4.8}$ .

Two distinct scaling laws of the slip velocity  $U_s$  with the wall shear stress  $\tau_w$  are observed when the flow rates are increased past the full plug regime. Within the partially yielded flow regime, a power-law scaling of the slip velocity with the wall shear stress is observed,  $U_s \propto \tau_w^{3.5}$ , as shown by the full line in Fig. 8(a). Within the fully yielded flow regime, the scaling becomes linear,  $U_s \propto \tau_w$ , as shown by the dashed line Fig. 8(a). For both the partially yielded and fully yielded regimes, a power-law scaling of the slip velocity with the wall velocity gradients  $\frac{dU}{dy}|_w$  is observed [Fig. 8(b)].

The physical reasons behind the emergence of a power-law scaling for the physical quantities relevant in describing the wall slip behavior remain elusive. A power-law scaling is often a signature of hierarchical organization in a complex system, which in this case is the microstructure of the Carbopol gel during yielding. The implicit hypothesis underpinning our work is that the phenomenon of wall slip is intrinsically dependent on the fluid microstructural changes during yielding. Since it was demonstrated that the yielding of a yield stress material may be understood as a bifurcation phenomenon (or a phase transition) [25,37], we may suggest that the wall slip exhibits a similar behavior and hence a similar mathematical structure, which justifies the use of a power law to fit the experimental data. Unfortunately, the constraints dictated by the physical system under consideration allow us to validate the power-law behavior only over a limited range of the parameter values, which is an issue of which we are fully aware.

Through the last part of the paper, we have investigated the effectiveness of a chemical treatment proposed by Métivier and co-workers in Ref. [53] in removing the wall slip effects. Whereas the treatment is indeed able to remove the wall slip effects during macrorheological tests (Fig. 10), its effectiveness at a microscopic scale is somewhat more limited. First, although the treatment is able to inhibit the wall slip effects (the slip velocities are smaller and the wall velocity gradients significantly larger), it does not completely remove them [Fig. 11(a)]. A second drawback of the chemical treatment relates to the emergence of secondary flow due to the presence of solid blobs attached to the walls of the microchannel at positions randomly distributed downstream (Fig. 14). Third, the temporal stability of this treatment is limited: after a week, the effects of the treatment vanished and the macroscopic slip behavior was fully restored (see the squares in Fig. 10).

The results presented in this study clearly call for both experimental and theoretical studies along several lines. On the experimental side, future studies that could capture the evolution of the microstructure of the yield material with the flow would help to clarify the generally accepted (but, to the best of our knowledge, not demonstrated experimentally) picture of a thin depleted layer of solvent in the vicinity of the solid surface. This is a rather difficult task, as it requires

the development of a chemical reaction that can graft a low molar mass fluorescent compound on the microstructural units of the gel without altering its yield stress behavior. An important step in this direction has been made only very recently by designing a chemical reaction that is able to covalently stain the Carbopol structural units with rhodamine, which allows one to visualize the dynamics of the solid microstructure during microscopic flows [43]. The preliminary visualization of the Carbopol microstructure illustrated in Fig. 10 of Ref. [43] seems to rule out the presence of a layer of solvent, which, as discussed throughout the paper, is the cornerstone of most of the existing scaling theories for the wall slip.

Along theoretical lines, in order to understand the physical mechanisms of the wall slip, one needs to develop a micromechanical framework that can describe the dynamics of the solid/fluid material units in close proximity to the solid wall, which in turn would allow one to predict analytical laws for the scaling of the slip velocity with the wall shear stresses. Lastly, such a physical picture of the wall slip needs to be incorporated later in a novel constitutive law that can fully describe confined flows in the presence of slip.

### ACKNOWLEDGMENTS

We acknowledge the Agence Nationale de la Recherche (ANR) for the financial support via project NaiMYS (ANR-16-CE06-0003). V.B. gratefully acknowledges a visiting fellowship from Polytech Nantes. E.Y. and T.B. are deeply indebted to Georgios C. Georgiou for valuable discussions on flows of yield stress fluids in the presence of wall slip.

- 
- [1] M. Cloître, *Advance in Polymer Science 236, High Solid Dispersions* (Springer-Verlag, Berlin, 2010).
  - [2] M. Cloître and R. T. Bonnecaze, A review of wall slip in high solid suspensions, *Rheol. Acta* **56**, 283 (2017).
  - [3] P. Tabeling, Phénomènes de glissement à l'interface liquide-solide, *C. R. Phys.* **5**, 531 (2004).
  - [4] J.-H. J. Cho, B. M. Law, and F. Rieutord, Dipole-Dependent Slip of Newtonian Liquids at Smooth Solid Hydrophobic Surfaces, *Phys. Rev. Lett.* **92**, 166102 (2004).
  - [5] P. Panaseti, A.-L. Vayssade, G. C. Georgiou, and M. Cloitre, Confined viscoplastic flows with heterogeneous wall slip, *Rheol. Acta* **56**, 539 (2017).
  - [6] Y. Damianou, G. Kaoullas, and G. C. Georgiou, Cessation of viscoplastic poiseuille flow in a square duct with wall slip, *J. Non-Newtonian Fluid Mech.* **233**, 13 (2016), papers presented at the Rheology Symposium in honor of Prof. R. I. Tanner on the occasion of his 82nd birthday, in Vathi, Samos, Greece.
  - [7] S. P. Meeker, R. T. Bonnecaze, and M. Cloitre, Slip and Flow in Soft Particle Pastes, *Phys. Rev. Lett.* **92**, 198302 (2004).
  - [8] J. R. Seth, M. Cloitre, and R. T. Bonnecaze, Influence of short-range forces on wall-slip in microgel pastes, *J. Rheol.* **52**, 1241 (2008).
  - [9] P. Ballesta, R. Besseling, L. Isa, G. Petekidis, and W. C. K. Poon, Slip and Flow of Hard-Sphere Colloidal Glasses, *Phys. Rev. Lett.* **101**, 258301 (2008).
  - [10] P. Ballesta, G. Petekidis, L. Isa, W. C. K. Poon, and R. Besseling, Wall slip and flow of concentrated hard-sphere colloidal suspensions, *J. Rheol.* **56**, 1005 (2012).
  - [11] X. Zhang, E. Lorenceau, P. Basset, T. Bourouina, F. Rouyer, J. Goyon, and P. Coussot, Wall Slip of Soft-Jammed Systems: A Generic Simple Shear Process, *Phys. Rev. Lett.* **119**, 208004 (2017).
  - [12] T. Divoux, V. Lapeyre, V. Ravaine, and S. Manneville, Wall slip across the jamming transition of soft thermoresponsive particles, *Phys. Rev. E* **92**, 060301 (2015).
  - [13] D. Germain and M. Le Merrer, Bubbles slipping along a crenelated wall, *Europhys. Lett.* **115**, 64005 (2016).
  - [14] A. Poumaere, M. Moyers-Gonzalez, C. Castelain, and T. Burghelaa, Unsteady laminar flows of a carbopol gel in the presence of wall slip, *J. Non-Newtonian Fluid Mech.* **205**, 28 (2014).

- [15] J. Pérez-González, J. J. López-Durán, B. M. Marín-Santibáñez, and F. Rodríguez-González, Rheo-piv of a yield-stress fluid in a capillary with slip at the wall, *Rheol. Acta* **51**, 937 (2012).
- [16] D. M. Kalyon, Apparent slip and viscoplasticity of concentrated suspensions, *J. Rheol.* **49**, 621 (2005).
- [17] V. Bertola, F. Bertrand, H. Tabuteau, D. Bonn, and P. Coussot, Wall slip and yielding in pasty materials, *J. Rheol.* **47**, 1211 (2003).
- [18] Y. Liu, D. Lorusso, D. W. Holdsworth, T. L. Poehpping, and J. R. de Bruyn, Effect of confinement on the rheology of a yield-stress fluid, *J. Non-Newtonian Fluid Mech.* **261**, 25 (2018).
- [19] B. Geraud, L. Bocquet, and C. Barentin, Confined flows of a polymer microgel, *Eur. Phys. J. E* **36**, 30 (2013).
- [20] A.-L. Vayssade, C. Lee, E. Terriac, F. Monti, M. Cloitre, and P. Tabeling, Dynamical role of slip heterogeneities in confined flows, *Phys. Rev. E* **89**, 052309 (2014).
- [21] J. Péméja, B. Géraud, C. Barentin, and M. Le Merrer, Wall slip regimes in jammed suspensions of soft microgels, *Phys. Rev. Fluids* **4**, 033301 (2019).
- [22] V. Bertola, Wicking with a yield stress fluid, *J. Phys.: Condens. Matter* **21**, 035107 (2009).
- [23] G. German and V. Bertola, The spreading behavior of capillary driven yield-stress drops, *Colloids Surf., A* **366**, 18 (2010).
- [24] G. German and V. Bertola, Formation of viscoplastic drops by capillary breakup, *Phys. Fluids A* **22**, 033101 (2010).
- [25] T. Burghelea and V. Bertola, *Transport Phenomena in Complex Fluids* (Springer International, 2019).
- [26] E. Kaliviotis, J. M. Sherwood, and S. Balabani, Local viscosity distribution in bifurcating microfluidic blood flows, *Phys. Fluids A* **30**, 030706 (2018).
- [27] A.-L. Vayssade, Flows of Herschel-Bulkley fluids in confined environments: Applications to the cementing of oil wells, Ph.D. thesis, l'Université Pierre et Marie Curie (2015).
- [28] J. R. Seth, C. Locatelli-Champagne, F. Monti, R. T. Bonnecaze, and M. Cloitre, How do soft particle glasses yield and flow near solid surfaces? *Soft Matter* **8**, 140 (2012).
- [29] V. Mansard, L. Bocquet, and A. Colin, Boundary conditions for soft glassy flows: slippage and surface fluidization, *Soft Matter* **10**, 6984 (2014).
- [30] S. G. Hatzikiriakos, Slip mechanisms in complex fluid flows, *Soft Matter* **11**, 7851 (2015).
- [31] S. G. Hatzikiriakos, Wall slip of molten polymers, *Prog. Polym. Sci.* **37**, 624 (2012), topical Issue on Polymer Physics.
- [32] S. Curran, R. Hayes, A. Afacan, M. Williams, and P. Tanguy, Properties of carbopol solutions as models for yield-stress fluids, *J. Food Sci.* **67**, 176 (2002).
- [33] G. Ovarlez, S. Cohen-Addad, K. Krishan, J. Goyon, and P. Coussot, On the existence of a simple yield stress fluid behavior, *J. Non-Newtonian Fluid Mech.* **193**, 68 (2013), viscoplastic Fluids: From Theory to Application.
- [34] J. Piau, Carbopol gels: Elastoviscoplastic and slippery glasses made of individual swollen sponges: Meso- and macroscopic properties, constitutive equations and scaling laws, *J. Non-Newtonian Fluid Mech.* **144**, 1 (2007).
- [35] T. Divoux, D. Tamarii, C. Barentin, and S. Manneville, Transient Shear Banding in a Simple Yield Stress Fluid, *Phys. Rev. Lett.* **104**, 208301 (2010).
- [36] A. M. V. Putz and T. I. Burghelea, The solid-fluid transition in a yield stress shear thinning physical gel, *Rheol. Acta* **48**, 673 (2009).
- [37] T. Burghelea, M. Moyers-Gonzalez, and R. Sainudiin, A nonlinear dynamical system approach for the yielding behavior of a viscoplastic material, *Soft Matter* **13**, 2024 (2017).
- [38] E. Weber, M. Moyers-Gonzalez, and T. I. Burghelea, Thermorheological properties of a carbopol gel under shear, *J. Non-Newtonian Fluid Mech.* **183-184**, 14 (2012).
- [39] M. M. Gonzalez, T. Burghelea, and J. Mak, Linear stability analysis for plane-poiseuille flow of an elastoviscoplastic fluid with internal microstructure for large reynolds numbers, *J. Non-Newtonian Fluid Mech.* **166**, 515 (2011).
- [40] F. K. Oppong and J. R. de Bruyn, Diffusion of microscopic tracer particles in a yield-stress fluid, *J. Non-Newtonian Fluid Mech.* **142**, 104 (2007).

- [41] I. A. Gutowski, D. Lee, J. de Bruyn, and B. Frisken, Scaling and mesostructure of carbopol dispersions, *Rheol. Acta* **51**, 441 (2012).
- [42] R. Sainudiin, M. Moyers-Gonzalez, and T. Burghelca, A microscopic gibbs field model for the macroscopic yielding behavior of a viscoplastic fluid, *Soft Matter* **11**, 5531 (2015).
- [43] E. Younes, M. Himl, Z. Stary, V. Bertola, and T. Burghelca, On the elusive nature of carbopol gels: “model”, weakly thixotropic, or time-dependent viscoplastic materials? *J. Non-Newtonian Fluid Mech.* **281**, 104315 (2020).
- [44] T. Thorsen, S. J. Maerkl, and S. R. Quake, Microfluidic large-scale integration, *Science* **298**, 580 (2002).
- [45] F. Scarano and M. L. Rhiethmuller, Advances in iterative multigrid piv image processing, *Exp. Fluids* **29**, S051 (2001).
- [46] M. Raffel, C. E. Willert, S. T. Wereley, and J. Kompenhans, *Particle Image Velocimetry: A Practical Guide (Experimental Fluid Mechanics)*, 2nd ed. (Springer, 2007).
- [47] H. A. Barnes, A review of the slip (wall depletion) of polymer solutions, emulsions and particle suspensions in viscometers: its cause, character, and cure, *J. Non-Newtonian Fluid Mech.* **56**, 221 (1995).
- [48] L. Ferrás, J. Nóbrega, and F. Pinho, Analytical solutions for newtonian and inelastic non-newtonian flows with wall slip, *J. Non-Newtonian Fluid Mech.* **175-176**, 76 (2012).
- [49] Y. Damianou, M. Philippou, G. Kaoullas, and G. C. Georgiou, Cessation of viscoplastic poiseuille flow with wall slip, *J. Non-Newtonian Fluid Mech.* **203**, 24 (2014).
- [50] S. P. Meeker, R. T. Bonnecaze, and M. Cloitre, Slip and flow in pastes of soft particles: Direct observation and rheology, *J. Rheol.* **48**, 1295 (2004).
- [51] T. Jiang, A. Young, and A. Metzner, The rheological characterization of hpg gels: Measurement of slip velocities in capillary tubes, *Rheol. Acta* **25**, 397 (1986).
- [52] F. Kitagawa, K. Kubota, K. Sueyoshi, and K. Otsuka, One-step immobilization of cationic polymer onto a poly(methyl methacrylate) microchip for high-performance electrophoretic analysis of proteins, *Sci. Technol. Adv. Mater.* **7**, 558 (2006).
- [53] C. Metivier, Y. Rharbi, A. Magnin, and A. Bou Abboud, Stick-slip control of the carbopol microgels on polymethyl methacrylate transparent smooth walls, *Soft Matter* **8**, 7365 (2012).
- [54] F. K. Oppong, L. Rubatat, B. J. Frisken, A. E. Bailey, and J. R. de Bruyn, Microrheology and structure of a yield-stress polymer gel, *Phys. Rev. E* **73**, 041405 (2006).